

1 **Impact of trench retreat rate on initiating focused back-arc extension within a mobile**  
2 **overriding plate**

3 Zhibin Lei<sup>1</sup>, J. Huw Davies<sup>1</sup>

4 <sup>1</sup>School of Earth and Environmental Sciences, Cardiff University, Cardiff, CF10 3AT, UK

5 Correspondence to: Zhibin Lei ([leiz2@cardiff.ac.uk](mailto:leiz2@cardiff.ac.uk))

6 Author Twitter handles: [@Lei\\_geodynamics](https://twitter.com/Lei_geodynamics)

7 Highlights:

8 1. Investigate dynamic internally driven subduction models with mobile overriding plate

9 2. Self-consistently produce high trench retreat rate and rifting, even in mobile plates

10 3. A minimum trench retreat rate is required to initiate rifting of the back-arc region

11 4. Back-arc extension arises from non-uniform basal drag induced by rapid trench retreat

---

This manuscript has been submitted to *Earth and Planetary Science Letters* and it is currently under review. This version has not undergone peer review and subsequent versions of this manuscript may have slightly different content. If accepted, the final version of this manuscript will be accessible via the “Peer-reviewed Publication DOI” link on the right-hand side of this webpage.

---

**13 Abstract**

14 Rapid trench retreat, or slab roll-back, is often observed in subduction zones where active and  
15 focused back-arc extension develops. However, the correlation between trench retreat rate and  
16 back-arc extension has not been rigorously tested. Here we study the correlation by investigating  
17 a series of 2-D thermo-mechanical and internally driven numerical models with a mobile overriding  
18 plate in set-ups that lead to a wide range of trench retreat rate. The results produced three grades  
19 of localised back-arc stretching states as the trench retreat rate increases: i) minor extension with  
20 observable but not significant thinning of the thermal lithosphere; ii) rifting extension with hot mantle  
21 thermally intruded upward to the surface; iii) new spreading seafloor with thin lithosphere. We find  
22 that it takes a minimum trench retreat rate to initiate rifting extension in the back-arc. The extension  
23 is driven by the non-uniform basal drag of the trenchward mantle wedge flow due to rapid trench  
24 retreat. The results could potentially be used to explain the southward decreasing stretching state  
25 along the Lau-Havre-Taupo back-arc system where trench retreat rate decreases southward as  
26 well. On the other hand, in the models we find that an older subducting plate leads to faster trench  
27 retreat rate, but this correlation only exists before the slab approaches the lower mantle. This  
28 matches well with the observation that the subducting plate age is always old (>55 Ma) in  
29 subduction zones with back-arc extension. It also explains why there is a poor correlation between  
30 the age of subducting plate and trench retreat rate because most slabs have already reached the  
31 lower mantle.

32 **Keywords:** subduction; trench retreat; back-arc; rifting; basal drag; numerical modeling.

## 33 **1. Introduction**

34 The extension observed within the overriding plate in different subduction zones varies, especially  
35 in the back-arc. The extension ranges from inactive extension with high heat flow, e.g. Southeast  
36 Aleutian Basin (Christeson and Barth, 2015), to a rifting ridge with thinning lithosphere, e.g. Central  
37 Andaman Basin, Taupo Volcanic Zone (Morley and Alvey, 2015; Parson and Wright, 1996), and  
38 further extended to the opening of a new oceanic floor, e.g. Sea of Japan, Lau Basin (Jolivet et al.,  
39 1994; Taylor et al., 1996). The extension plays a significant role in producing hazards (Kósik et al.,  
40 2020) and generating resources (Fouquet et al., 1991; Hessler and Sharman, 2018), but the  
41 underlying driving mechanism is poorly understood.

42 Observation of plate and trench motion shows that retreating trench correlates well with the  
43 existence of back-arc extension except for some cases where trench retreat rate is lower than 5  
44 cm/yr (Heuret and Lallemand, 2005; Schellart et al., 2008). A general explanation for this correlation  
45 is that the overriding plate extends to accommodate the void that trench retreat leaves. In detail,  
46 two driving mechanisms have been proposed: trench retreat generates strong convection currents  
47 (poloidal and toroidal flow) that transmits non-uniform basal traction upon the overriding plate  
48 (Sleep and Toksöz, 1971); and trench suction at the subduction zone interface pulls the overriding  
49 plate (Elsasser, 1971).

50 Further observations of subducting systems with a high trench retreat rate shows that a localised  
51 extension often develops in the overriding plate. For example, the trench retreat rate at Tonga is  
52 ~16 cm/yr where we observe spreading ridge and opening seafloor (Bevis et al., 1995). The  
53 correlation is supported by numerical and analogue investigations. Both trench retreat induced

54 poloidal and toroidal flow components show a positive correlation with trench retreat rate (Funicello  
55 et al., 2004; Stegman et al., 2006). Models with a higher trench retreat rate also correlates with  
56 higher strain rate in the overriding plate (Holt et al., 2015; Meyer & Schellart, 2013). On the other  
57 hand, previous research indicates that the trailing boundary condition and heterogeneity of the  
58 overriding plate also play important roles in affecting the degree of back-arc extension. Models with  
59 either a fixed overriding plate or an overriding plate containing an arbitrary weak zone are prone to  
60 produce rifting or spreading back-arc extension (Capitanio et al., 2010; Gerya et al., 2008; Herten  
61 et al., 2020; Nakakuki and Mura, 2013; Yang et al., 2019), while studies with a mobile and  
62 homogeneous (without an arbitrary weak zone) overriding plate often fail to produce an opening  
63 back-arc incorporating focused thinning lithosphere (Chen et al., 2016; Čížková and Bina, 2013;  
64 Schellart and Moresi, 2013). To summarise, rigorous investigation has not been done yet on the  
65 trench retreat rate's role in initiating different extents of back-arc extension, especially within a  
66 mobile and homogeneous overriding plate.

67 In this research, we ran a series of 2-D thermo-mechanical and self-consistently driven models with  
68 a mobile overriding plate in set-ups that lead to a wide range of trench retreat rate. The results  
69 produced three different types of localised back-arc stretching states as the trench retreat rate  
70 increases: i) minor extension with observable but not significant thinning of the thermal lithosphere;  
71 ii) rifting extension with hot mantle thermally intruded upward to the surface; iii) new spreading  
72 seafloor with thin lithosphere. We find that a minimum trench retreat rate is needed to initiate rifting  
73 extension in the back-arc. The extension is driven by the non-uniform basal drag of the trenchward  
74 mantle wedge flow due to rapid trench retreat.

## 75 2. Methods

76 Extending the model setup of Garel et al. (2014), we ran a series of 2-D thermally-driven subduction  
 77 models using the code Fluidity (Davies et al., 2011; Kramer et al., 2012), a finite-element control-  
 78 volume computational modelling framework, with an adaptive mesh that can capture evolving  
 79 changes with a maximum resolution of 0.4 km. To obtain a wide range of trench retreat rate for a  
 80 mobile overriding plate, we vary the initial age of the subducting plate at the trench.

### 81 2.1 Governing equations

82 Under the Boussinesq approximation (McKenzie et al., 1974), the equations governing thermally  
 83 driven subduction process are derived from conservation of mass, momentum, and energy, for an  
 84 incompressible Stokes flow

$$85 \quad \partial_i u_i = 0, \quad (1)$$

$$86 \quad \partial_i \sigma_{ij} = -\Delta \rho g_j, \quad (2)$$

$$87 \quad \frac{\partial T}{\partial t} + u_i \partial_i T = \kappa \partial_i^2 T, \quad (3)$$

88 in which  $u$ ,  $g$ ,  $\sigma$ ,  $T$ ,  $\kappa$  are the velocity, gravity, stress, temperature, and thermal diffusivity,  
 89 respectively (Table 1). In particular, the full stress tensor  $\sigma_{ij}$  consists of deviatoric and lithostatic  
 90 components via

$$91 \quad \sigma_{ij} = \tau_{ij} - p \delta_{ij}, \quad (4)$$

92 where  $\tau_{ij}$  represents the deviatoric stress tensor,  $p$  the dynamic pressure, and  $\delta_{ij}$  the Kronecker  
 93 delta function.

94 Table 1. Key parameters used in this research

Quantity	Symbol	Units	Value
Gravity	$g$	$m s^{-2}$	9.8
Gas constant	$R$	$J K^{-1} mol^{-1}$	8.3145
Mantle geothermal gradient	$G$	$K km^{-1}$	0.5 (UM) 0.3 (LM)
Thermal expansivity coefficient	$\alpha$	$K^{-1}$	$3 \times 10^{-5}$
Thermal diffusivity	$\kappa$	$m^2 s^{-1}$	$10^{-6}$
Reference density	$\rho_s$	$kg m^{-3}$	3300
Cold, surface temperature	$T_s$	$K$	273
Hot, mantle temperature	$T_m$	$K$	1573
Maximum viscosity	$\mu_{max}$	$Pa s$	$10^{25}$
Minimum viscosity	$\mu_{min}$	$Pa s$	$10^{18}$
<b>Diffusion Creep</b>			
Activation energy	$E$	$kJ mol^{-1}$	300 (UM) 200 (LM)
Activation volume	$V$	$cm^3 mol^{-1}$	4 (UM) 1.5 (LM)
Prefactor	$A$	$Pa^{-n} s^{-1}$	$3.0 \times 10^{-11}$ (UM) $6.0 \times 10^{-17}$ (LM)
	$n$		1
<b>Dislocation Creep (UM)</b>			
Activation energy	$E$	$kJ mol^{-1}$	540
Activation volume	$V$	$cm^3 mol^{-1}$	12
Prefactor	$A$	$Pa^{-n} s^{-1}$	$5.0 \times 10^{-16}$
	$n$		3.5
<b>Peierls Creep (UM)</b>			
Activation energy	$E$	$kJ mol^{-1}$	540
Activation volume	$V$	$cm^3 mol^{-1}$	10
Prefactor	$A$	$Pa^{-n} s^{-1}$	$10^{-150}$
	$n$		20
<b>Yield Strength Law</b>			
Surface yield strength	$\tau_0$	$MPa$	2
Friction coefficient	$f_c$		0.2
	$f_{c,weak}$		0.02 (weak layer)
Maximum yield strength	$\tau_{y,max}$	$MPa$	10,000

96 The deviatoric stress tensor and strain rate tensor  $\dot{\epsilon}_{ij}$  are related according to

$$97 \quad \tau_{ij} = 2\mu\dot{\epsilon}_{ij} = \mu(\partial_j u_i + \partial_i u_j), \quad (5)$$

98 with  $\mu$  the viscosity. The density difference due to temperature is defined as

$$99 \quad \Delta\rho = -\alpha\rho_s(T - T_s), \quad (6)$$

100 where  $\alpha$  is the coefficient of thermal expansion,  $\rho_s$  is the reference density at the surface  
101 temperature  $T_s$  (Table 1).

## 102 **2.2 Rheology**

103 The governing rheological laws are identical throughout the model domain, though the rheology  
104 parameters we use may differ to match different deformation mechanisms observed at different  
105 depths in the Earth. In detail, a uniform composite viscosity is used to take account of four  
106 deformation mechanisms under different temperature-pressure conditions: diffusion creep,  
107 dislocation creep, Peierls mechanism, and yielding (Garel et al., 2014). The effective composite  
108 viscosity in the computational domain is given by

$$109 \quad \mu = \left( \frac{1}{\mu_{diff}} + \frac{1}{\mu_{disl}} + \frac{1}{\mu_P} + \frac{1}{\mu_y} \right)^{-1}, \quad (7)$$

110 where  $\mu_{diff}$ ,  $\mu_{disl}$ ,  $\mu_y$  define the creep viscosity following

$$\mu_{diff/disl/P} = A^{-\frac{1}{n}} \exp\left(\frac{E + PV}{nRT_r}\right) \dot{\epsilon}_{II}^{\frac{1-n}{n}}, \quad (8)$$

in which  $A$  is a prefactor,  $n$  the stress component,  $E$  the activation energy,  $P$  the lithostatic pressure,  $V$  the volume,  $R$  the gas constant,  $T_r$  the temperature obtained by adding an adiabatic gradient of 0.5 K/km in the upper mantle and 0.3 K/km in the lower mantle to the Boussinesq solution (Fowler, 2005),  $\dot{\epsilon}_{II}$  the second invariant of the strain rate tensor. While the fourth deformation mechanism, yielding, is defined by a brittle-failure type yield-stress law as

$$\mu_y = \frac{\tau_y}{2\dot{\epsilon}_{II}}, \quad (9)$$

with  $\mu_y$  the yielding viscosity and  $\tau_y$  the yield strength.  $\tau_y$  is determined by

$$\tau_y = \min(\tau_0 + f_c P, \tau_{y,max}), \quad (10)$$

with  $\tau_0$  the surface yield strength,  $f_c$  the friction coefficient,  $P$  the lithostatic pressure, and  $\tau_{y,max}$  the maximum yield strength (Table 1). Note the weak zone, a 5 km thick region on top of the subducting plate, has the same rheology, except its value of  $f_c$  is one tenth, and its maximum viscosity is  $10^{20}$  Pa s. We note that for all models in this research there is no arbitrary weak zone placed in the initial overriding plate.

### 2.3 Model setup

Following Garel et al., 2014, we run spatially large models where the computational domain is 10000 km by 2900 km, with  $x$  (width) coordinates and  $z$  (depth) coordinates extending from the surface to the bottom of the lower mantle. Such a wide domain reduces the influence of side and

129 bottom boundary conditions (Chertova et al., 2012). The thermal boundary conditions at the surface  
 130 and bottom are defined by two isothermal values:  $T = T_s$  and  $T = T_m$  for surface and base of  
 131 lower mantle respectively, while the sidewalls are insulating. As for velocity boundary conditions, a  
 132 free-surface is applied at the top boundary to enable trench mobility, while the other boundaries are  
 133 free-slip.

134  $Age_{SP}^0$  and  $Age_{OP}^0$  represent the initial ages of subducting plate and overriding plate at the trench,  
 135 which starts in the middle of the surface. Laterally on the surface, the age of both plates increases  
 136 linearly with its distance away from the mid-ocean ridge on either side. While vertically, the age of  
 137 plate at surface defines the initial thermal structure through a half-space cooling model (Turcotte  
 138 and Schubert, 2002),

$$139 \quad T(x, z) = T_s + (T_m - T_s) \operatorname{erf} \left( \frac{z}{2\sqrt{\kappa Age^0(x)}} \right), \quad (11)$$

140 with  $x$  the distance away from the mid-ocean ridge,  $z$  the depth,  $\kappa$  the thermal diffusivity. The  
 141 thermal lithosphere is defined as the material colder than 1300 K.

142 The free surface boundary condition together with the mid-ocean ridge setup allow the subducting  
 143 slab, overriding plate and trench to move freely as subduction evolves. To allow for a self-driven  
 144 subduction without implementing external forces, the subducting plate is set up with a bend into the  
 145 mantle and a 5 km thick low-viscosity decoupling layer on the top. The initial bending radius is 250  
 146 km and the slab bends over 77 degrees from the trench (Figure 1).

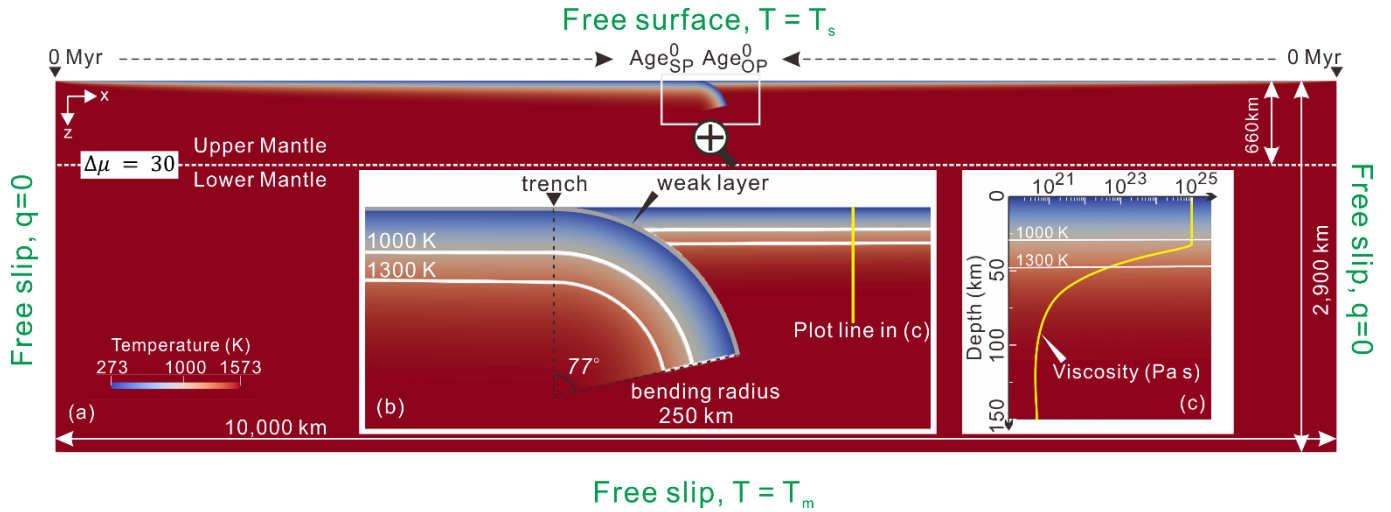


Figure 1. Model geometry and initial setup illustrated with the initial temperature field as the background.  $Age_{SP}^0$  and  $Age_{OP}^0$  represent the initial ages of subducting plate and overriding plate at trench. The viscosity jump ( $\Delta\mu$ ) between upper and lower mantle at 660km transition zone is set up with a fixed value of 30. The trench is recognised as the position where the overriding plate meets the weak layer coating the subducting plate at the surface. a) The whole computational domain. b) Enlarged area of trench zone where bending slab meets flat overriding plate. A 5 km thick weak layer is set up on top of the subducting slab to facilitate decoupling. 1100 K and 1300 K isotherms are marked in white lines. c) Vertical profile of viscosity against depth within the overriding plate. The plot line is 400 km away from the initial trench.

## 2.4 Modify the rate of trench retreat

Trench retreat rate is related to multiple factors. Numerical investigations have shown that older subducting plate or higher slab density (Alsaif et al., 2020; Garel et al., 2014), narrower trench width (Schellart et al., 2011; Stegman et al., 2006), the inclusion of overriding plate and its aspect ratio (Butterworth et al., 2012; Capitanio et al., 2010), younger overriding plate or thinner overriding plate (Garel et al., 2014; Hertgen et al., 2020), and less slab resistance to bending (Di Giuseppe et al., 2008) could all contribute to stronger trench retreat. While a higher viscosity jump at the mantle transition zone (Čížková and Bina, 2013; Garel et al., 2014), and a stress-dependent mantle viscosity (Holt & Becker, 2017) could reduce the rate of trench retreat.

Of all the parameters, the plate age turns out to be a concise and efficient parameter to obtain a wide range of trench retreat rate in our model set-up. In detail, we only modify the initial plate ages

166 ( $Age_{SP}^0$  and  $Age_{OP}^0$ ) at the trench (Table 2), which varies the net negative buoyancy of the hanging  
 167 slab and determines the maximum trench retreat rate potential during subduction. Meanwhile,  
 168 several diagnostics were used to monitor the trench motion during the 10 Myr long simulations.  
 169 Two series of models, each series with the same  $Age_{OP}^0$  and a growing  $Age_{SP}^0$ , are simulated to  
 170 demonstrate the role trench retreat rate may play in generating different extent of localised  
 171 extension in the back-arc region.

172 Table 2. List of representative models with key variables governing trench retreat rate and diagnostics monitoring the trench motion  
 173 and stretching state of the overriding plate.

Model name	$Age_{SP}^0$ (Myr)	$Age_{OP}^0$ (Myr)	$H_{SP}^0$ (km)	$H_{OP}^0$ (km)	$t_{660}$ (Myr)	$ \Delta x_{trench}^{0-t_{660}} $ (km)	$ u_{max}^{0-t_{660}} $ (cm/yr)	$ \overline{u_{trench}^{0-t_{660}}} $ (cm/yr)	Back-arc stretching state
SP80_OP20	80	20	89	45	3.8	138	11	3.6	i
SP90_OP20	90	20	94	45	3.5	160	14	4.6	i
SP100_OP20	100	20	100	45	3.2	200	19	6.3	ii
SP125_OP20	125	20	111	45	2.8	340	65	12.1	iii
SP150_OP20	150	20	122	45	2.5	390	113	15.6	iii
SP100_OP25	100	25	100	50	4.1	145	10	3.5	i
SP125_OP25	125	25	111	50	3.7	168	14	4.5	i
SP150_OP25	150	25	122	50	3.5	200	20	5.7	i
SP175_OP25	175	25	132	50	3.3	250	27	7.6	ii
SP200_OP25	200	25	141	50	3.1	375	96	12.1	iii

174 Models are named as follows, e.g. SP80\_OP20 corresponds to initial subducting plate age at the trench of 80 Myr and 20 Myr for  
 175 overriding plate.  $H_{SP}^0$  and  $H_{OP}^0$  are the initial thermal lithosphere thickness, marked by 1300 K isotherm, of the subducting plate and  
 176 overriding plate at trench separately.  $t_{660}$  equals how much time the subducting plate takes to sink to 660km depth.  $|\Delta x_{trench}^{0-t_{660}}|$  is  
 177 the total trench retreat in the period of  $t_{660}$ .  $|u_{max}^{0-t_{660}}|$  and  $|\overline{u_{trench}^{0-t_{660}}}|$  are the magnitude of maximum and average trench retreat rate  
 178 recorded during  $t_{660}$ . The code i, ii and iii describing the back-arc stretching state of the overriding plate represents minor extension,  
 179 rifting and new spreading seafloor, respectively.

180 With a wide range of trench retreat rates achieved, we will be able to investigate its influence on  
 181 the formation of different extents of extension within the overriding plate.

### 3. Results

#### 3.1 Trench retreat rate through time

Self-consistent subduction, in most numerical and analogue models, starts with a non-steady state where negative buoyancy pulls the slab into the deeper mantle (eg. Capitanio et al., 2010; Gerya et al., 2008; Schellart and Moresi, 2013). Meanwhile, trench retreat accelerates with time and reaches a maximum value ( $u_{max}^{0-t_{660}}$ ) when the slab starts to interact with the lower mantle at  $t_{660}$  (Figure 2-a). During the interaction, the viscosity jump at  $\sim 660$  km provides a balanced competing upward support to the sinking slab, as a result the trench retreat experiences an abrupt deceleration due to the reducing slab pull force. After this short period of adjustment, subduction enters the second stage, a near steady state where trench retreat rate keeps a constant magnitude at  $\sim 3$  cm/yr for all the models.

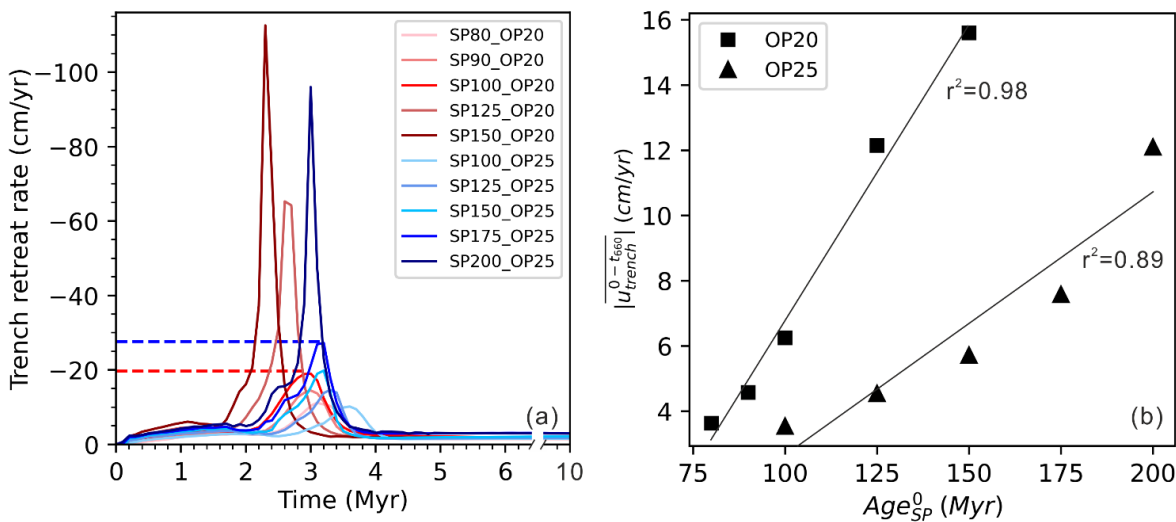
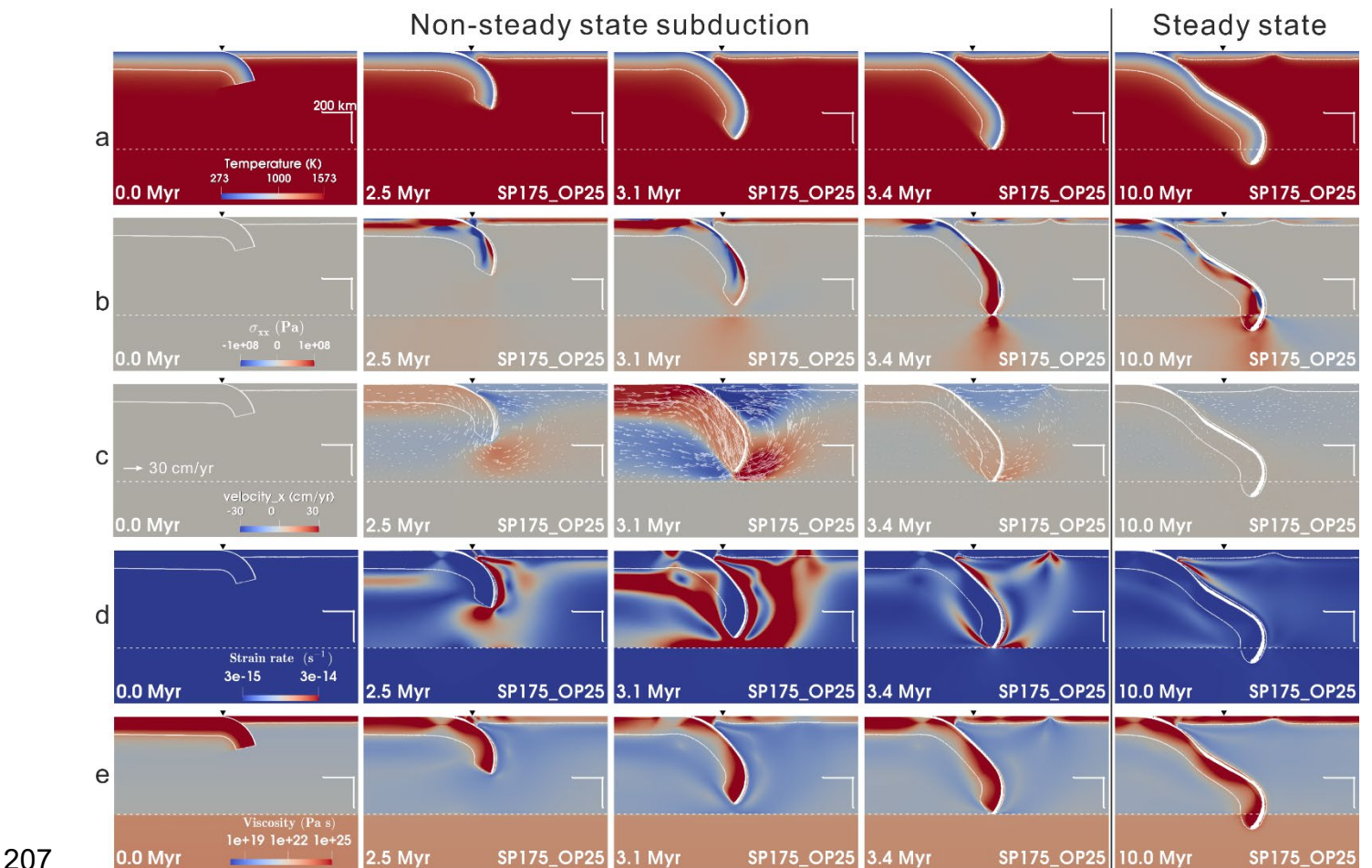


Figure 2. The motion of the trench through time and its  $Age_{Sp}^0$  dependency during non-steady state subduction. a) Trench retreat rate through time. Negative value means that the trench is moving towards the subducting plate. The dashed lines of red and blue marks the  $u_{max}^{0-t_{660}}$  for model SP100\_OP20 and SP175\_OP25 separately. b) Slab age dependency of diagnostic  $|u_{trench}^{0-t_{660}}|$  during non-steady state subduction.

198 For models with the same overriding plate setup, the average trench retreat rate over the first stage  
 199 ( $\overline{|u_{trench}^{0-t_{660}}|}$ ) is  $Age_{SP}^0$ -dependent during non-steady state subduction (Figure 2-b). However, this  
 200 dependence fades away when the slab starts to interact with the lower mantle (Figure 2-a).

### 201 3.2 Subduction kinematics

202 Starting from our segmentation of the subduction into non-steady and steady state subduction, we  
 203 investigate further to reveal more details of this model subduction system. Here using model  
 204 SP175\_OP25 as a case study, we characterise the whole process by illustrating the simultaneous  
 205 dynamic evolution of temperature, horizontal component of the stress field, horizontal component  
 206 of the velocity field, second invariant of strain rate, and magnitude of viscosity (Figure 3).



207  
 208 Figure 3. Simultaneous snapshots of a zoom-in to the region of active subduction in model SP175\_OP25 showing: a) temperature,

209 b) horizontal component of the stress field, positive is extensional stress while negative is compressional stress, c) horizontal  
210 component of velocity field superimposed with velocity vectors, d) second invariant of strain rate, e) magnitude of viscosity. The  
211 downward black triangle at the surface marks the initial location of trench. The curved white solid line underneath the plate is the  
212 1300 K isotherm, i.e., we take this as the bottom of the thermal lithosphere. The dashed white line marks the base of the transition  
213 zone at 660 km depth. The number with unit 'Myr' in the bottom left corner is the duration of the simulation. The right-angle scale  
214 bars above the transition zone represent 200 km in both horizontal and vertical direction.

### 215 *3.2.1 Non-steady state subduction*

216 Before the subducting plate starts to interact with the lower mantle around 3.3 Myr (Table 2), there  
217 is visible erosion in the mantle wedge (Figure 3-a). The horizontal component of the stress field  
218 indicates that the overriding plate portion away from the subducting plate is in a general high  
219 extensional stress field ( $> 50$  MPa), leaving the portion close to the subducting plate in a general  
220 compressional stress state (Figure 3-b). The velocity vectors visualise a clockwise laminar mantle  
221 flow underlying the subducting plate and an anticlockwise poloidal flow underlying the overriding  
222 plate (Figure 3-c). The horizontal component of velocity field within the whole overriding plate is  
223 initially consistent laterally. As the slab sinking accelerates, the trenchward velocity of the overriding  
224 plate next to the trench increases faster than the trailing part of the overriding plate. This creates  
225 an increasing horizontal velocity difference within the overriding plate. In the corresponding area, a  
226 high strain rate region (Figure 3-d) and low viscosity (Figure 3-e) region at 3.1-3.4 Myr is observed  
227 marking the initiation of the rifting within the overriding plate.

### 228 *3.2.2 Steady state subduction*

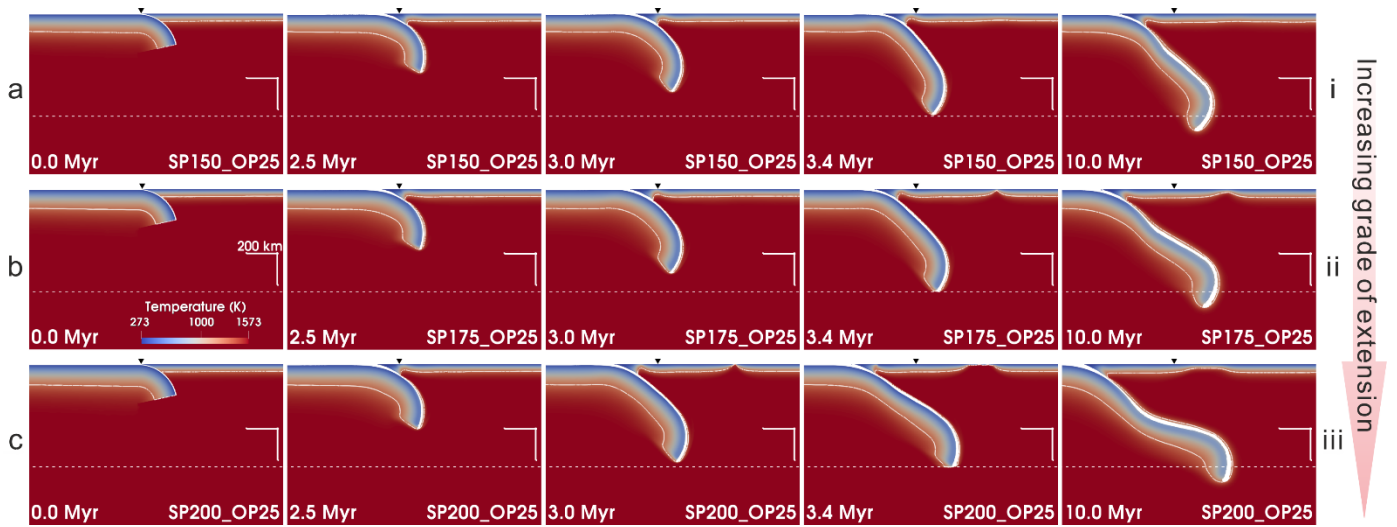
229 After the subducting plate reaches the lower mantle, both the mantle wedge erosion and the  
230 initiated rift cools down and the thermal thickness of the overriding plate starts to recover. The  
231 horizontal component of the stress field within the overriding plate loses the general high

232 extensional stress state and becomes mixed with a low magnitude of both compressional and  
233 extensional stress field. The velocity field indicates that the whole system decelerates to a slow-  
234 motion mode, where plates and mantle flow move with a low uniform velocity magnitude. Meanwhile,  
235 the high strain rate vanishes in the back-arc region and it is only observed in a limited area in the  
236 mantle wedge. The viscosity field within the overriding plate also recovers its stiffness. In summary,  
237 the mobility of the whole subduction system is inhibited in this stage and tectonics within the  
238 overriding plate is relatively silent compared with the non-steady state subduction stage.

### 239 **3.3 Three types of stretching state within the overriding plate**

240 The case described above has demonstrated the ability of a retreating trench to deform the  
241 overriding plate. Here we present the diversity of localised extension that trench retreat can bring  
242 about within the overriding plate. Three grades of stretching state within the overriding plate have  
243 been recognised (Table 2). Grade i) Minor extension. In the mantle wedge, convective mantle flux  
244 erodes part of the overriding plate's bottom (Figure 4-a). Further away towards the overriding plate,  
245 observable but very limited thinning of the thermal lithosphere develops. Grade ii) Rifting. A higher  
246 magnitude of thermal erosion develops in the mantle wedge. While rifting extension forms during  
247 non-steady state subduction in the back-arc (Figure 4-b). The rift goes inactive during the steady  
248 state subduction. Grade iii) Spreading seafloor or break-up extension. In the mantle wedge, even  
249 higher magnitude of thermal erosion develops but no rifting extension forms. Further away towards  
250 the overriding plate, rifting extension develops and then breaks up into two parts forming a new  
251 oceanic floor during non-steady state subduction (Figure 4-c). The width of the opening seafloor  
252 can be as wide as ~250 km. During the steady state subduction, the break-up goes inactive due to

253 the lack of consistent strong trench retreat.



254

255

256

257

Figure 4. Simultaneous snapshots of the thermal field evolution of three cases, illustrating the differing stretching states within the overriding plate: a) minor extension (model SP150\_OP25); b) rifting (model SP175\_OP25); c) spreading seafloor (model SP200\_OP25). All screenshots share the same temperature scale as is shown in first screenshot in row b.

258

259

260

261

262

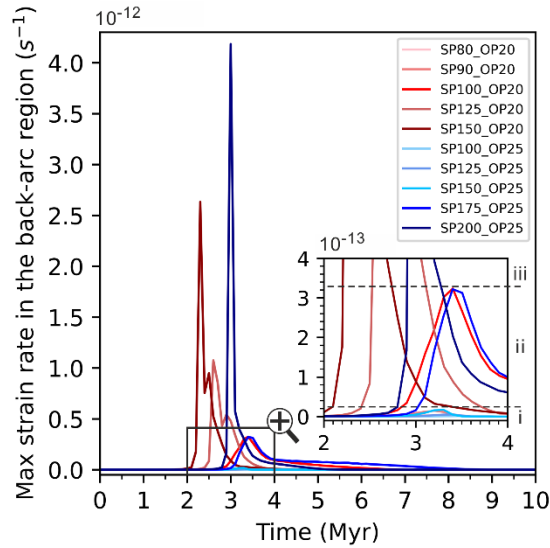
263

264

265

266

To understand the deformation in the three stretching states, we track the second invariant of strain rate ( $\dot{\epsilon}_{II}$ ) in the back-arc region and plot it over time (Figure 5). It shows that for the five models that develop minor extension stretching state (Table 2),  $\dot{\epsilon}_{II}$  is always less than  $2 \times 10^{-14} s^{-1}$  throughout the simulation. While for the two rifting extension models,  $\dot{\epsilon}_{II}$  can go beyond  $2 \times 10^{-14} s^{-1}$  and reach the maximum value of  $\sim 3.3 \times 10^{-13} s^{-1}$  when rift develops within the overriding plate. For the three break-up models,  $\dot{\epsilon}_{II}$  exceeds  $3.3 \times 10^{-13} s^{-1}$  when the rifting ridge starts to spread in the back-arc. The strain rate quickly drops down to less than  $1 \times 10^{-13} s^{-1}$  during steady state subduction, indicating that extensional deformation within the overriding plate gradually stops simultaneously.



267

268

269

270

Figure 5. Maximum second invariant of strain rate through time in the back-arc region. The period from 2 to 4 Myr is enlarged to display the maximum strain rate corresponding to minor extension (Grade i) and to rift extension (Grade ii) that can be achieved throughout the simulation.

271

272

273

274

275

276

277

278

Matching the three stretching states with the trench retreat rate over time (Figure 2-a), we note that it takes a minimum magnitude of trench retreat rate ( $u_{\text{rift}}$ ) to initiate rifting within a given overriding plate. The  $u_{\text{rift}}$  for  $Age_{OP}^0 = 20 \text{ Myr}$  and  $Age_{OP}^0 = 25 \text{ Myr}$  are  $\sim 19 \text{ cm/yr}$  and  $\sim 27 \text{ cm/yr}$  respectively. When the trench retreat rate exceeds  $u_{\text{rift}}$ , break-up extension develops following the rifting in the back-arc region. Take model SP200\_OP25 for example, when the trench retreat rate reaches  $\sim 27 \text{ cm/yr}$  at 2.9 Myr, the overriding plate starts to rift and  $\dot{\epsilon}_{II}$  is  $1.8 \times 10^{-13} \text{ s}^{-1}$  falling in the range of rift deformation (Figure 5). Then the trench retreat rate exceeds  $u_{\text{rift}}$  and break-up extension develops characterised by high  $\dot{\epsilon}_{II}$  greater than  $3.3 \times 10^{-13} \text{ s}^{-1}$  (Figure 5).

279

### 3.4 Regime diagram

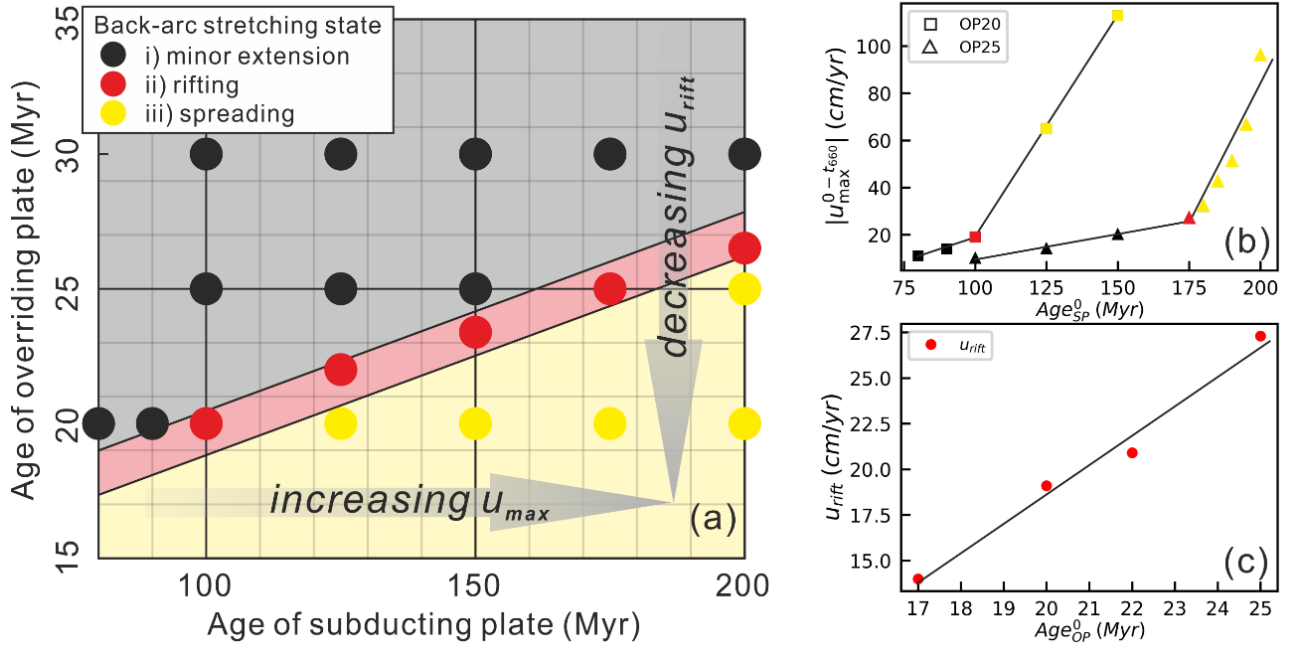
280

281

282

Combining the above diagnostics and visualised output, we plot a regime diagram of overriding plate stretching state in response to different model setup (Figure 6-a). The diagram is divided into three parts based on the final stretching state of the overriding plate: i) minor extension, ii) rifting,

283 iii) spreading new seafloor. The diagram shows that with either increasing  $Age_{SP}^0$  (i.e., increasing  
 284  $|u_{max}^{0-t_{660}}|$ ) or decreasing  $Age_{OP}^0$  (i.e., decreasing  $u_{rift}$ ), a stronger extent of extension develops  
 285 within the back-arc region.



286  
 287 Figure 6. Regime diagram of back-arc extension and age dependency of trench motions. (a) Regime diagram of back-arc stretching  
 288 state with varying  $Age_{SP}^0$  and  $Age_{OP}^0$ . Grey area with black dot models has minor extension in the back-arc region, while pink area  
 289 with red dot models is rifting extension. The yellow area with gold dot models represents spreading back-arc. (b) The maximum  
 290 trench retreat rate in response to  $Age_{SP}^0$ . (c) The minimum trench retreat rate to initiate rift extension within an overriding plate with  
 291 an initial age of  $Age_{OP}^0$ . The colour of markers in (b) and (c) refer to the legend of back-arc stretching state in (a).

292 In summary, we propose that it takes a minimum magnitude of trench retreat rate  $u_{rift}$  to initiate  
 293 rifting within a given overriding plate in these models. The  $|u_{max}^{0-t_{660}}|$  depends on  $Age_{SP}^0$  for a given  
 294 overriding plate (Figure 6-b), while the magnitude of  $u_{rift}$  depends on the strength of the overriding  
 295 plate, i.e.  $Age_{OP}^0$  in this research (Figure 6-c). A steeper slope of  $|u_{max}^{0-t_{660}}|$  against  $Age_{SP}^0$  is  
 296 observed in models with spreading extension (Figure 6-b). This suggests that the strength of the  
 297 original overriding plate is greatly weakened during rift extension and it becomes equivalent to a  
 298 much younger overriding plate in terms of rheology.

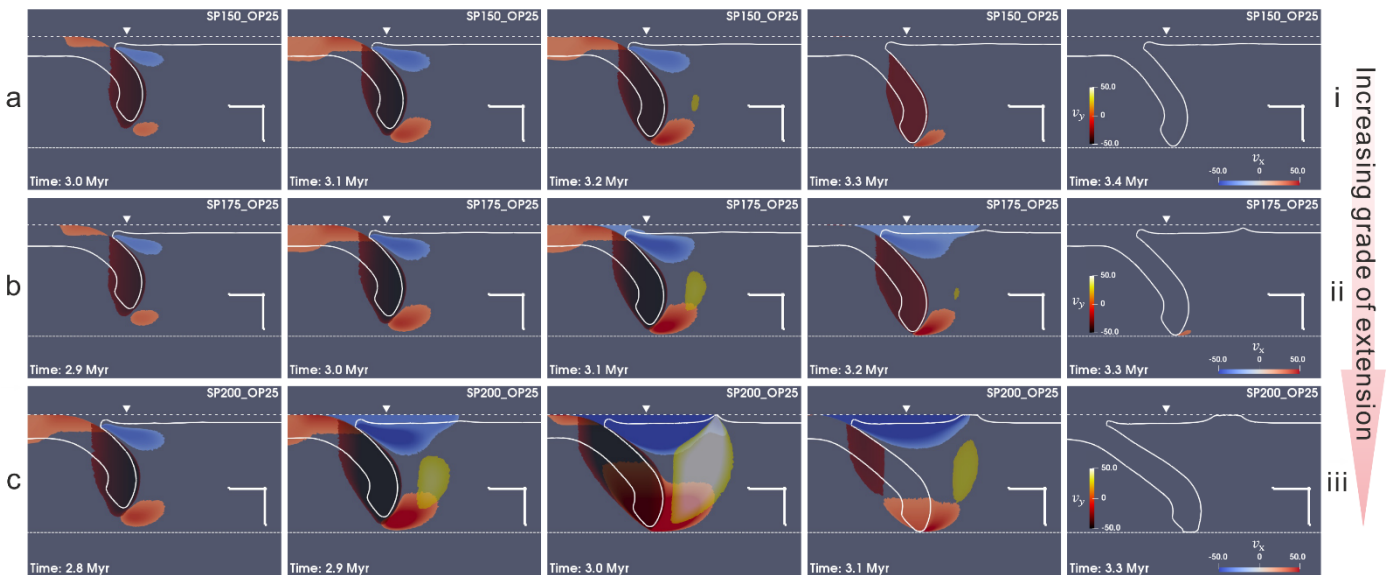
299 Comparing  $|u_{max}^{0-t_{660}}|$  and  $u_{rift}$ , we find that the results match well with the stretching state  
 300 observed. i) If  $u_{max} < u_{rift}$  then the overriding plate lithosphere has little extension and max  $\dot{\epsilon}_{II}$  is  
 301  $3 \times 10^{-14} s^{-1}$ . ii) If  $u_{max} \approx u_{rift}$  the overriding plate rifts but would neither be torn apart nor spread,  
 302 when  $\dot{\epsilon}_{II}$  ranges from  $3 \times 10^{-14} s^{-1}$  to  $3 \times 10^{-13} s^{-1}$ . iii) If  $u_{max} > u_{rift}$ , the back-arc region rifts  
 303 when the trench retreat rate reaches  $u_{rift}$ , then it breaks up into two parts and spreads after it  
 304 exceeds  $u_{rift}$  with  $\dot{\epsilon}_{II}$  simultaneously exceeding  $3 \times 10^{-13} s^{-1}$ .

## 305 **4. Discussion**

### 306 **4.1 Origin of the three stretching states in the overriding plate**

307 The driving mechanism of how the trench retreats, and slab rollback induces extension within the  
 308 overriding plate remains debated. Trench suction and non-uniform basal traction are two basic  
 309 driving mechanisms. The stress field results show that a compressional stress field next to the  
 310 subduction interface on the overriding plate's side prevails during the non-steady state subduction  
 311 (Figure 3-b). This indicates that shortening, rather than extension, is the dominant deformation  
 312 there, which excludes a direct correlation between trench suction at the subduction interface with  
 313 focused back-arc extension. Similar shortening deformation at the subduction interface as the  
 314 trench retreats is also reported in other research (Chen et al., 2016; Schellart and Moresi, 2013).  
 315 However, the velocity field does show that mantle flow underlying the overriding plate is sucked  
 316 into the wedge as the slab rolls back (Figure 3-c). So 'deep slab suction' rather than 'trench suction'  
 317 may contribute to the back-arc extension by facilitating the mobility of mantle flow in the mantle  
 318 wedge.

319 To understand the origin of the three overriding plate stretching states developed in this research,  
 320 we need to study the mantle circulation underlying the overriding plate. During the non-steady state  
 321 subduction, a strong anticlockwise poloidal flow develops underlying the overriding plate before the  
 322 rift forms (Figure 3-c). Take models SP150\_OP25, SP175\_OP25 and SP200\_OP25 for example,  
 323 the flow could be decomposed into two components: focused upwelling from the transition zone;  
 324 and trenchward horizontal flow underneath the overriding plate (Figure 7). These two differently  
 325 directed flows correspond to the two end members of potential driving mechanisms accounting for  
 326 the stretching state within the overriding plate: 1) upwelling thermal intrusion; and 2) lateral basal  
 327 traction. As velocity difference is key to generate shear traction upon the overriding plate, we select  
 328 the high velocity component areas ( $\geq u_{rift}$ ) and analyse their correlation with the development of  
 329 three stretching states within the overriding plate.



330  
 331 Figure 7. Snapshots of vertical and horizontal components of mantle circulation induced by slab roll-back. The vertical flow ( $u_y$ ) and  
 332 horizontal flow ( $u_x$ ) are highlighted with two separate color legends (right most snapshot). Trenchward and downwelling motions are  
 333 negative in the screenshots. Besides, all the visualised areas have a velocity magnitude higher than  $u_{rift}$  ( $\sim 27$  cm/yr for  $Age_{OP}^0 =$   
 334  $25$  Myr) in the corresponding direction, i.e. either  $|u_y| \geq u_{rift}$ , or  $|u_x| \geq u_{rift}$ . The models i, ii, iii corresponds to the three stretching  
 335 states described in Figure 4. The loose dashed line marks the surface while the dense dashed line is at 660 km depth (the base of  
 336 the transition zone).

337 *4.1.1 Lateral basal traction*

338 The fast horizontal flow prevails over the upwelling component among all snapshots in figure 7.  
339 Initially, the trenchward horizontal flow forms in the mantle wedge underlying the overriding plate  
340 and extends laterally to ~500 km from the wedge corner (Figure 7). The spatial distribution indicates  
341 the existence of both lateral and vertical velocity gradient, which produce non-uniform magnitude  
342 of basal drag beneath the overriding plate. The wedge flow gradually drags the overlying overriding  
343 plate trenchward. This can be seen as the high velocity magnitude region extends up from the  
344 wedge to include the overriding plate (3.1 to 3.2 Myr in Figure 7-b and 2.8 to 3.1 Myr in Figure 7-  
345 c). Due to the non-uniform basal drag effect, the trenchward velocity difference within the overriding  
346 plate grows. This leads to a growing magnitude of accumulated extension which would end up with  
347 increasing stretching states within the overriding plate.

348 The magnitude of the horizontal flow can exceed 50 cm/yr for a short period (<1 Myr) in these  
349 models. Seismic anisotropy observations near slab edges beneath Tonga and Alaska subduction  
350 zones suggest comparable magnitude of rapid wedge flow, up to 90 cm/yr (Conder and Wiens,  
351 2007; Jadamec and Billen, 2010). Here we propose that the non-uniform basal drag of the rapid  
352 wedge flow driven by rapid trench retreat plays a vital role in producing back-arc opening during  
353 subduction.

354 *4.1.2 Upwelling thermal intrusion*

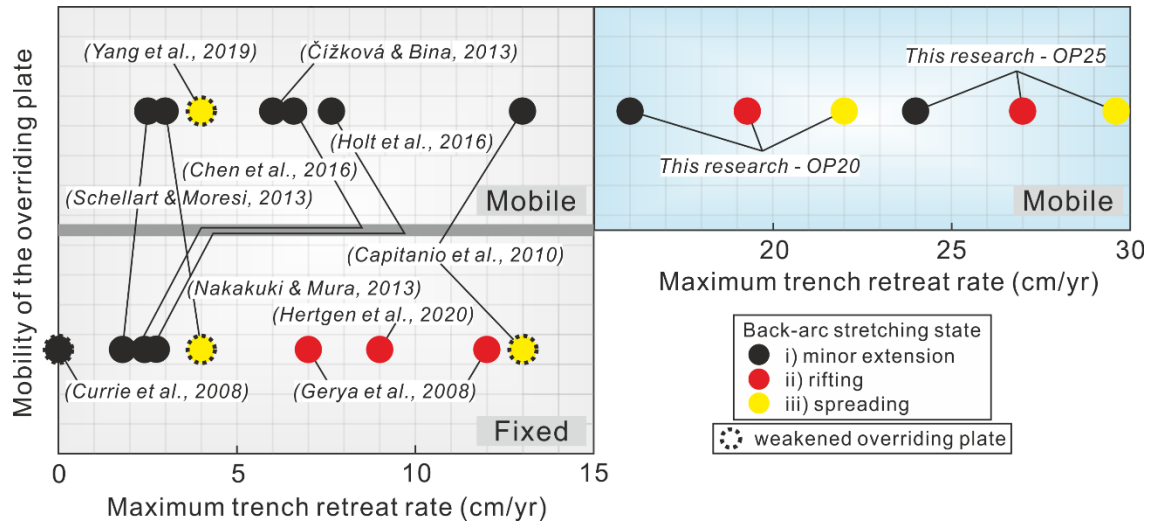
355 Figure 7 shows that fast-upwelling mantle flow is observed in all three models though it lasts for no  
356 more than 0.3 Myr. The size of the fast-upwelling mantle body grows with  $Age_{SP}^0$ , indicating a

357 stronger return flow. In model SP200\_OP25, the upwelling even appears under the rift before it  
358 fades away as the non-steady state subduction ends (Figure 7-c). However, the high velocity  
359 upwelling flow is prone to strengthen the stretching within the overriding plate rather than initiating  
360 significant rifting extension. We state this because it is not observed to interact with the overriding  
361 plate for model SP175\_OP25 which starts to rift at 3.2 Myr (Figure 7-b).

362 In summary, the basal traction induced by trench retreat, or slab rollback, is the main driving force  
363 to account for different magnitude of extension within the overriding plate in our models. While the  
364 upwelling mantle component may reinforce the extension.

#### 365 **4.2 Comparing with other back-arc extension models**

366 Previous research indicates that fixing the trailing boundary condition of the overriding plate can  
367 increase the degree of focused back-arc extension in contrast to models with a free mobile  
368 overriding plate (Capitanio et al., 2010; Chen et al., 2016; Hertgen et al., 2020; Nakakuki and Mura,  
369 2013; Schellart and Moresi, 2013). While introducing heterogeneity, e.g. weak zone, in the  
370 overriding plate (Currie et al., 2008; Nakakuki and Mura, 2013; Yang et al., 2019) or lowering the  
371 strength of the whole overriding plate (Capitanio et al., 2010) can cultivate thinning lithosphere or  
372 even spreading back-arc extension (Figure 8). In brief, it usually takes a fixed or a weakened  
373 overriding plate to produce back-arc extension incorporating a rift. By contrast, this research  
374 demonstrates the capability of producing an opening back-arc in a homogeneous (i.e. without an  
375 arbitrary weak zone) mobile overriding plate by increasing the magnitude of non-uniform basal drag  
376 underlying the overriding plate as the trench retreats rapidly.



377

378

Figure 8. Summary of maximum trench retreat rate, mobility of the overriding plate and back-arc stretching state in previous research.

379

Previous models also indicate that maximum trench retreat is often reached at the end of non-

380

steady state subduction when the slab starts to interact with the lower mantle (eg. Capitanio et al.,

381

2010; Schellart and Moresi, 2013). The maximum trench retreat rate achieved during previous

382

research presented in Figure 8 is ~13 cm/yr, which is lower than that of ~16 cm/yr observed in

383

Tonga (Bevis et al., 1995). Considering that more than 90% of slabs have reached the lower mantle

384

(van der Meer et al., 2018), the non-steady state subduction is transient relative to the following

385

steady state subduction and its evolving history is poorly constrained by observations. Here we

386

consider that the trench retreat rate can reach a high magnitude, at least for a short period (<1 Myr),

387

during the non-steady state subduction phase, as produced in our models. This allows us to

388

suggest the existence of a minimum trench retreat rate to initiate back-arc opening for a given

389

overriding plate. The results imply that the role of non-steady state subduction and transient rapid

390

trench retreat in promoting deformation within the overriding plate may be underestimated.

391

### 4.3 Comparing with subduction zones on Earth

392

Our results indicates that when the age of the subducting slab is old enough, it will allow the trench

393 to retreat fast enough to initiate rift extension or even break-up extension in the back-arc region  
394 through non-uniform basal traction. This may explain why the subducting plate is always old,  
395 ranging from 55 Ma – 160 Ma, in subduction zones with a back-arc basin (Sdrolias and Müller,  
396 2006).

397 We obtain a wide range of trench retreat rate by tuning  $Age_{SP}^0$ . However, modern observation  
398 shows that there is poor correlation between  $Age_{SP}^0$  and trench retreat rate (Heuret and Lallemand,  
399 2005). Our result indicates that trench retreat rate loses its age dependency when the subducting  
400 slab starts to interact with the lower mantle. Considering that most subducting slabs on Earth have  
401 already reached or are approaching the lower mantle (van der Meer et al., 2018), it is then not  
402 surprising that a poor correlation is observed. The result suggests that different stages of  
403 subduction play an important role in controlling subduction kinematics and it may help us better  
404 understand observations on Earth.

405 We replicate three back-arc stretching states with a wide range of trench retreat rate. The extent of  
406 back-arc extension exhibits positive correlation with trench retreat rate. This matches well with  
407 subduction zones where trench retreat rates are higher than 5 cm/yr on Earth (Heuret and  
408 Lallemand, 2005; Schellart et al., 2008). Take the Lau-Havre-Taupo back-arc system for example,  
409 the width of the back-arc region narrows southward from ~500 km in Lau Basin to ~100 km along  
410 the Havre Trough and terminates in Taupo Volcanic Zone (Parson and Wright, 1996). The trench  
411 retreat rate correspondingly slows down from ~16 cm/yr to ~0 cm/yr along the Tonga-Kermadec  
412 trench (Schellart et al., 2008). While the thickness of the crust increases from ~5 km to ~25 km  
413 southward (Parson and Wright, 1996) and a high spreading rate is observed in northern Lau Basin

414 at  $\sim 9.1 - 15.9$  cm/yr (Bevis et al., 1995).

415 In our models that produce spreading back-arc, we find that the opening seafloor stops spreading  
416 after trench retreat rate drops to a low constant magnitude of  $\sim 3$  cm/yr during steady state  
417 subduction (Figure 4-c). This may explain why some spreading back-arc stop spreading even when  
418 subduction continues. For example, the back-arc in Japan sea opened at  $\sim 21$  Ma and ceased  
419 spreading since  $\sim 14$  Ma during the Pacific Plate subduction (Tatsumi et al., 1990). The Japan  
420 subduction zone is still active while the present trench retreat rate is low at only  $\sim 0$  cm/yr (Schellart  
421 et al., 2008).

422 We noted, our simplified models cannot reproduce the periodic opening process of the back-arc  
423 basin. Magnetic anomalies in opening back-arc regions indicate that the spreading tends to be  
424 periodic and consistent (Caratori Tontini et al., 2019; Eagles and Jokat, 2014) rather than abrupt  
425 and short-lived. During steady state subduction, the rifted back-arc region is likely to spread if high  
426 trench retreat rate is maintained rather than drops to the value of  $\sim 3$  cm/yr seen in our models. This  
427 may be attributed to the limitation imposed by our 2D models which is discussed next.

## 428 **4.4 Limitations**

### 429 *4.4.1 2D and 3D models*

430 Trench retreat could generate convective mantle flow that includes poloidal and toroidal  
431 components. Two dimensional models, by their nature, can only produce poloidal flow. It is noted  
432 though, that poloidal flow is expected to dominate during the non-steady state subduction

433 (Funiciello et al., 2004). That is when high trench retreat rate develops in our models. Thus, a lack  
434 of toroidal flow might only have a limited impact on the formation of rapid trench retreat rate during  
435 non-steady state subduction.

436 However, as the subducting slab starts to interact with the lower mantle, trench retreat and upper  
437 mantle flow in 2D models are greatly inhibited (Figure 2-a, Figure 3-c). Trench retreat rate slows  
438 down by ~60% (Holt et al., 2015) and >70% in our models. This occurs because the subducting  
439 slab, combining with the viscosity jump into the lower mantle, disconnects the upper mantle flow  
440 on either side of the slab. While in 3D models, toroidal flow could efficiently transport mantle flow  
441 from the subducting plate side towards the overriding plate side - around the edges of slabs. Slab  
442 interaction with the lower mantle only slows down the trench retreat by 0% to ~33% in 3D models  
443 (Chen et al., 2016; Schellart et al., 2011). In this case where the slab is interacting with the lower  
444 mantle, the lack of toroidal flow causes a significant slowing down effect on the trench retreat rate  
445 and potentially also simultaneously inhibits back-arc extension. Thus, the lack of toroidal flow may  
446 not be neglected when slab starts to interact with the lower mantle.

#### 447 *4.4.2 Absolute value of trench retreat rate and $u_{rift}$*

448 This research aims to provide a guiding reference framework to correlate trench retreat rate and  
449 extent of extension in the back-arc region rather than provide precise predictions. Thus, the  
450 absolute value of trench retreat rate should be treated with caution. We note that while the older  
451 subducting plate ages (> 160 Ma) at trenches are presently not common on Earth (Müller et al.,  
452 2008), they provide us a way to self-consistently produce the varying trench retreat rates.  
453 Considering that there is a lot of uncertainty in terms of the strength of plates on Earth, the trench

454 retreat rate it takes to initiate rift extension could vary greatly. Some of our models yield much higher  
 455 trench retreat rates than observed, this may imply that either the rheology we used does not fully  
 456 agree with real Earth or that current observation might be incomplete.

457 During non-steady state subduction,  $\left| \overline{u_{trench}^{0-t_{660}}} \right|$  in our model (3.5-15.6 cm/yr) is in the same range  
 458 as actual observations on Earth (0-16 cm/yr). While the maximum trench retreat rate obtained from  
 459 the model (10-113 cm/yr) spans a much wider range than observations on Earth. The extremely  
 460 high  $|u_{max}^{0-t_{660}}|$  is achieved in spreading back-arc models after the back-arc lithosphere's rheology  
 461 is reshaped by the emplaced rifting ridge. Similar abrupt acceleration is reported to exist in some  
 462 rifting continental margins and it is controlled by the nonlinear decay of the strength force resisting  
 463 rifting (Brune et al., 2016).

464 The  $u_{rift}$  for  $Age_{OP}^0 = 20 Myr$  and  $Age_{OP}^0 = 25 Myr$  are  $\sim 19$  cm/yr and  $\sim 27$  cm/yr separately,  
 465 hinting that it can be difficult to initiate rifting extension in models  $Age_{OP}^0 > 20 Myr$  with observed  
 466 trench retreat rates on Earth. There are several parameters that could potentially lower the  $u_{rift}$   
 467 which is not addressed in this research, for example, inhibiting the mobility of the overriding plate  
 468 or lowering the strength of the overriding plate.

## 469 5. Conclusion

470 The 2D thermo-mechanical self-consistent models demonstrate the capability of initiating back-arc  
 471 rifting or spreading in a mobile and homogenous (no arbitrary weak zone) overriding plate with high  
 472 enough trench retreat rate during subduction. A wide range of trench retreat rate is achieved by  
 473 varying the initial age of the subducting plate at the trench for a given overriding plate. The models

474 evolve from a non-steady state towards a steady state with the transition occurring when the  
475 subducting plate approaches the lower mantle. During non-steady state subduction, trench retreat  
476 rate accelerates and reaches its maximum value, which depends on the initial age of the subducting  
477 plate. In all, three types of stretching state were observed within the overriding plate: i) minor  
478 extension, where the overriding plate lithosphere remained generally unchanged; ii) rift extension,  
479 where the overriding plate would be rifted but not torn apart; iii) spreading extension, where back-  
480 arc is rifted and then breaks apart into two spreading parts. The results indicate that it takes a  
481 minimum trench retreat rate to initiate rift extension and a higher trench retreat rate to open the  
482 back-arc. The driving force in these models is suggested to be the non-uniform basal drag resulting  
483 from the mantle wedge flow driven by the rapid trench retreat. After the subducting plate reaches  
484 the lower mantle, the trench retreat rate drops to a constant magnitude around 3 cm/yr and loses  
485 the dependency on the initial age of subducting plate. Meanwhile, simultaneously the back-arc  
486 extension stops when trench retreat rate slows down during the steady state subduction. This  
487 suggests that different stages of subduction play an important role in controlling subduction  
488 kinematics and it may help us better understand why there is poor correlation between trench  
489 retreat rate and the age of subducting plate.

490 In addition to the previous understanding of back-arc extension, we propose that high enough  
491 trench retreat rate can initiate a rift or spreading back-arc extension through non-uniform basal drag  
492 even when the overriding plate is mobile.

493 **Code availability**

494 The numerical code, Fluidity, is open source and available from <https://fluidityproject.github.io/>.

495 **Acknowledgement**

496 Duo Zhang provided constructive suggestions. We acknowledge the support of Advanced  
497 Research Computing at Cardiff (ARCCA) and the Supercomputing Wales project, which is part-  
498 funded by the European Regional Development Fund (ERDF) via the Welsh Government. Zhibin  
499 Lei also thanks the China Scholarship Council (CSC) for supporting the Ph.D. studentship and  
500 Cardiff University for an overseas fee waiver award.

501 **References**

502 Alsaif, M., Garel, F., Gueydan, F., Davies, D.R., 2020. Upper plate deformation and trench retreat modulated by  
503 subduction-driven shallow asthenospheric flows. *Earth Planet. Sci. Lett.* 532.  
504 <https://doi.org/10.1016/j.epsl.2019.116013>

505 Bevis, M., Taylor, F.W., Schutz, B.E., Recy, J., Isacks, B.L., Helu, S., Singh, R., Kendrick, E., Stowell, J., Taylor, B.,  
506 Calmantli, S., 1995. Geodetic observations of very rapid convergence and back-arc extension at the tonga arc.  
507 *Nature* 374, 249–251. <https://doi.org/10.1038/374249a0>

508 Brune, S., Williams, S.E., Butterworth, N.P., Müller, R.D., 2016. Abrupt plate accelerations shape rifted continental  
509 margins. *Nature* 536, 201–204. <https://doi.org/10.1038/nature18319>

- 510 Butterworth, N.P., Quevedo, L., Morra, G., Müller, R.D., 2012. Influence of overriding plate geometry and rheology on  
511 subduction. *Geochemistry, Geophys. Geosystems* 13, 1–15. <https://doi.org/10.1029/2011GC003968>
- 512 Capitanio, F.A., Stegman, D.R., Moresi, L.N., Sharples, W., 2010. Upper plate controls on deep subduction, trench  
513 migrations and deformations at convergent margins. *Tectonophysics* 483, 80–92.  
514 <https://doi.org/10.1016/j.tecto.2009.08.020>
- 515 Caratori Tontini, F., Bassett, D., de Ronde, C.E.J., Timm, C., Wysoczanski, R., 2019. Early evolution of a young back-  
516 arc basin in the Havre Trough. *Nat. Geosci.* 12, 856–862. <https://doi.org/10.1038/s41561-019-0439-y>
- 517 Chen, Z., Schellart, W.P., Strak, V., Duarte, J.C., 2016. Does subduction-induced mantle flow drive backarc extension?  
518 *Earth Planet. Sci. Lett.* 441, 200–210. <https://doi.org/10.1016/j.epsl.2016.02.027>
- 519 Chertova, M. V., Geenen, T., Van Den Berg, A., Spakman, W., 2012. Using open sidewalls for modelling self-consistent  
520 lithosphere subduction dynamics. *Solid Earth* 3, 313–326. <https://doi.org/10.5194/se-3-313-2012>
- 521 Christeson, G.L., Barth, G.A., 2015. Aleutian basin oceanic crust. *Earth Planet. Sci. Lett.* 426, 167–175.  
522 <https://doi.org/10.1016/j.epsl.2015.06.040>
- 523 Čížková, H., Bina, C.R., 2013. Effects of mantle and subduction-interface rheologies on slab stagnation and trench  
524 rollback. *Earth Planet. Sci. Lett.* 379, 95–103. <https://doi.org/10.1016/j.epsl.2013.08.011>
- 525 Conder, J.A., Wiens, D.A., 2007. Rapid mantle flow beneath the Tonga volcanic arc. *Earth Planet. Sci. Lett.* 264, 299–  
526 307. <https://doi.org/10.1016/j.epsl.2007.10.014>

- 527 Currie, C.A., Huisman, R.S., Beaumont, C., 2008. Thinning of continental backarc lithosphere by flow-induced  
528 gravitational instability. *Earth Planet. Sci. Lett.* 269, 436–447. <https://doi.org/10.1016/j.epsl.2008.02.037>
- 529 Davies, D.R., Wilson, C.R., Kramer, S.C., 2011. Fluidity: A fully unstructured anisotropic adaptive mesh computational  
530 modeling framework for geodynamics. *Geochemistry, Geophys. Geosystems* 12, n/a-n/a.  
531 <https://doi.org/10.1029/2011GC003551>
- 532 Di Giuseppe, E., Van Hunen, J., Funiciello, F., Faccenna, C., Giardini, D., 2008. Slab stiffness control of trench motion:  
533 Insights from numerical models. *Geochemistry, Geophys. Geosystems* 9, 1–19.  
534 <https://doi.org/10.1029/2007GC001776>
- 535 Eagles, G., Jokat, W., 2014. Tectonic reconstructions for paleobathymetry in Drake Passage. *Tectonophysics* 611, 28–  
536 50. <https://doi.org/10.1016/j.tecto.2013.11.021>
- 537 Elsasser, W.M., 1971. Sea-floor spreading as thermal convection. *J. Geophys. Res.* 76, 1101–1112.  
538 <https://doi.org/10.1029/JB076i005p01101>
- 539 Fouquet, Y., Stackelberg, U. Von, Charlou, J.L., Donval, J.P., Erzinger, J., Foucher, J.P., Herzig, P., Mühe, R., Soakai,  
540 S., Wiedicke, M., Whitechurch, H., 1991. Hydrothermal activity and metallogenesis in the Lau back-arc basin.  
541 *Nature* 349, 778–781. <https://doi.org/10.1038/349778a0>
- 542 Fowler, C., 2005. *The Solid Earth: An Introduction to Global Geophysics*. Cambridge Univ. Press, Cambridge, U. K.
- 543 Funiciello, F., Faccenna, C., Giardini, D., 2004. Role of lateral mantle flow in the evolution of subduction systems:  
544 Insights from laboratory experiments. *Geophys. J. Int.* 157, 1393–1406. <https://doi.org/10.1111/j.1365->

545

246X.2004.02313.x

546

Garel, F., Goes, S., Davies, D.R., Davies, J.H., Kramer, S.C., Wilson, C.R., 2014. Interaction of subducted slabs with

547

the mantle transition-zone: A regime diagram from 2-D thermo-mechanical models with a mobile trench and an

548

overriding plate. *Geochemistry, Geophys. Geosystems* 15, 1739–1765. <https://doi.org/10.1002/2014GC005257>

549

Gerya, T. V., Connolly, J.A.D., Yuen, D.A., 2008. Why is terrestrial subduction one-sided? *Geology* 36, 43–46.

550

<https://doi.org/10.1130/G24060A.1>

551

Hertgen, S., Yamato, P., Guillaume, B., Magni, V., Schliffke, N., Hunen, J., 2020. Influence of the thickness of the

552

overriding plate on convergence zone dynamics. *Geochemistry, Geophys. Geosystems* 21.

553

<https://doi.org/10.1029/2019GC008678>

554

Hessler, A.M., Sharman, G.R., 2018. Subduction zones and their hydrocarbon systems. *Geosphere* 14, 2044–2067.

555

<https://doi.org/10.1130/GES01656.1>

556

Heuret, A., Lallemand, S., 2005. Plate motions, slab dynamics and back-arc deformation. *Phys. Earth Planet. Inter.*

557

149, 31–51. <https://doi.org/10.1016/j.pepi.2004.08.022>

558

Holt, A.F., Becker, T.W., 2017. The effect of a power-law mantle viscosity on trench retreat rate. *Geophys. J. Int.* 208,

559

491–507. <https://doi.org/10.1093/gji/ggw392>

560

Holt, A.F., Becker, T.W., Buffett, B.A., 2015. Trench migration and overriding plate stress in dynamic subduction models.

561

*Geophys. J. Int.* 201, 172–192. <https://doi.org/10.1093/gji/ggv011>

- 562 Jadamec, M.A., Billen, M.I., 2010. Reconciling surface plate motions with rapid three-dimensional mantle flow around  
563 a slab edge. *Nature* 465, 338–341. <https://doi.org/10.1038/nature09053>
- 564 Jolivet, L., Tamaki, K., Fournier, M., 1994. Japan Sea, opening history and mechanism: a synthesis. *J. Geophys. Res.*  
565 99. <https://doi.org/10.1029/93jb03463>
- 566 Kósik, S., Bebbington, M., Németh, K., 2020. Spatio-temporal hazard estimation in the central silicic part of Taupo  
567 Volcanic Zone, New Zealand, based on small to medium volume eruptions. *Bull. Volcanol.* 82.  
568 <https://doi.org/10.1007/s00445-020-01392-6>
- 569 Kramer, S.C., Wilson, C.R., Davies, D.R., 2012. An implicit free surface algorithm for geodynamical simulations. *Phys.*  
570 *Earth Planet. Inter.* 194–195, 25–37. <https://doi.org/10.1016/j.pepi.2012.01.001>
- 571 McKenzie, D.P., Roberts, J.M., Weiss, N.O., 1974. Convection in the earth's mantle: towards a numerical simulation.  
572 *J. Fluid Mech.* 62, 465. <https://doi.org/10.1017/S0022112074000784>
- 573 Meyer, C., Schellart, W.P., 2013. Three-dimensional dynamic models of subducting plate-overriding plate-upper mantle  
574 interaction. *J. Geophys. Res. Solid Earth* 118, 775–790. <https://doi.org/10.1002/jgrb.50078>
- 575 Morley, C.K., Alvey, A., 2015. Is spreading prolonged, episodic or incipient in the Andaman Sea? Evidence from  
576 deepwater sedimentation. *J. Asian Earth Sci.* 98, 446–456. <https://doi.org/10.1016/j.jseaes.2014.11.033>
- 577 Müller, R.D., Sdrolias, M., Gaina, C., Roest, W.R., 2008. Age, spreading rates, and spreading asymmetry of the world's  
578 ocean crust. *Geochemistry, Geophys. Geosystems* 9, 1–19. <https://doi.org/10.1029/2007GC001743>

- 579 Nakakuki, T., Mura, E., 2013. Dynamics of slab rollback and induced back-arc basin formation. *Earth Planet. Sci. Lett.*  
580 361, 287–297. <https://doi.org/10.1016/j.epsl.2012.10.031>
- 581 Parson, L.M., Wright, I.C., 1996. The Lau-Havre-Taupo back-arc basin: A southward-propagating, multi-stage evolution  
582 from rifting to spreading. *Tectonophysics* 263, 1–22. [https://doi.org/10.1016/S0040-1951\(96\)00029-7](https://doi.org/10.1016/S0040-1951(96)00029-7)
- 583 Schellart, W.P., Moresi, L., 2013. A new driving mechanism for backarc extension and backarc shortening through slab  
584 sinking induced toroidal and poloidal mantle flow: Results from dynamic subduction models with an overriding  
585 plate. *J. Geophys. Res. Solid Earth* 118, 3221–3248. <https://doi.org/10.1002/jgrb.50173>
- 586 Schellart, W.P., Stegman, D.R., Farrington, R.J., Moresi, L., 2011. Influence of lateral slab edge distance on plate  
587 velocity, trench velocity, and subduction partitioning. *J. Geophys. Res. Solid Earth* 116, 1–15.  
588 <https://doi.org/10.1029/2011JB008535>
- 589 Schellart, W.P., Stegman, D.R., Freeman, J., 2008. Global trench migration velocities and slab migration induced upper  
590 mantle volume fluxes: Constraints to find an Earth reference frame based on minimizing viscous dissipation.  
591 *Earth-Science Rev.* 88, 118–144. <https://doi.org/10.1016/j.earscirev.2008.01.005>
- 592 Sdrolias, M., Müller, R.D., 2006. Controls on back-arc basin formation. *Geochemistry, Geophys. Geosystems* 7.  
593 <https://doi.org/10.1029/2005GC001090>
- 594 Sleep, N.H., Toksöz, M.N., 1971. Evolution of Marginal Basins. *Nature* 233, 548–550. <https://doi.org/10.1038/233548a0>
- 595 Stegman, D.R., Freeman, J., Schellart, W.P., Moresi, L., May, D., 2006. Influence of trench width on subduction hinge  
596 retreat rates in 3-D models of slab rollback. *Geochemistry, Geophys. Geosystems* 7, n/a-n/a.

597

<https://doi.org/10.1029/2005GC001056>

598

Tatsumi, Y., Maruyama, S., Nohda, S., 1990. Mechanism of backarc opening in the Japan Sea: role of asthenospheric

599

injection. *Tectonophysics* 181, 299–306. [https://doi.org/10.1016/0040-1951\(90\)90023-2](https://doi.org/10.1016/0040-1951(90)90023-2)

600

Taylor, B., Zellmer, K., Martinez, F., Goodliffe, A., 1996. Sea-floor spreading in the Lau back-arc basin. *Earth Planet.*

601

*Sci. Lett.* 144, 35–40. [https://doi.org/10.1016/0012-821x\(96\)00148-3](https://doi.org/10.1016/0012-821x(96)00148-3)

602

Turcotte, D.L., Schubert, G., 2002. *Geodynamics*. Cambridge Univ. Press, Cambridge, U. K.

603

van der Meer, D.G., van Hinsbergen, D.J.J., Spakman, W., 2018. Atlas of the underworld: Slab remnants in the mantle,

604

their sinking history, and a new outlook on lower mantle viscosity. *Tectonophysics* 723, 309–448.

605

<https://doi.org/10.1016/j.tecto.2017.10.004>

606

Yang, T., Moresi, L., Gurnis, M., Liu, S., Sandiford, D., Williams, S., Capitanio, F.A., 2019. Contrasted East Asia and

607

South America tectonics driven by deep mantle flow. *Earth Planet. Sci. Lett.* 517, 106–116.

608

<https://doi.org/10.1016/J.EPSL.2019.04.025>

609